Scale Dependence of Air–Sea Fluxes over the Western Equatorial Pacific

JIELUN SUN,* JAMES F. HOWELL,+ STEVEN K. ESBENSEN,+ L. MAHRT,+ CHRISTINE M. GREB,+ ROBERT GROSSMAN,# AND M. A. LEMONE@

*Program in Atmospheric and Oceanic Sciences, University of Colorado, Boulder, Colorado
+College of Oceanic and Atmospheric Sciences, Oregon State University, Corvallis, Oregon
#PAOS/APAS, University of Colorado, Boulder, Colorado
@MMM, NCAR,& Boulder, Colorado

(Manuscript received 21 August 1995, in final form 19 January 1996)

ABSTRACT

The goal of this study is to examine the horizontal scale dependence of vertical eddy flux in the tropical marine surface boundary layer and how this scale dependence of flux relates to the bulk aerodynamic relationship and the parameterization of subgrid-scale flux. The fluxes of heat, moisture, and momentum are computed from data collected from 27 NCAR Electra flight legs in TOGA COARE (The Tropical Ocean Global Atmosphere Coupled Ocean–Atmosphere Response Experiment) with flight elevations lower than 40 m and flight runs longer than 60 km. The dependence of the fluxes on two length scales are studied: the cutoff length scale, defining the averaging length over which mean components are obtained in order to partition field variables into mean and perturbation components; and the flux averaging length scale, defining the length over which products of perturbations are averaged in order to estimate vertical fluxes. Based on the characteristics of the scale dependence of fluxes, the total flux of each flight leg is partitioned into "turbulent," "large eddy," and "mesoscale" fluxes due to motions smaller than 1 km, between 1 and 5 km, and between 5 km and the flight leg length, respectively.

The results show that fluxes are sensitive to the choice of cutoff length scale in the presence of significant mesoscale activity and in the weak wind case where the turbulent fluxes are small. The turbulent momentum flux decreases with increasing flux averaging length scale due to mesoscale modulation of the turbulent stress vector.

Mesoscale heat, moisture, and momentum fluxes for individual flight legs can reach 20% of the turbulent fluxes in the presence of well-organized convective cloud systems even at 35 m above the sea surface. The mesoscale flux is less correlated to the wind speed and bulk air–sea difference than turbulent fluxes. The local mesoscale flux can be upward or downward, and therefore, its average value is reduced when averaging over a single flight leg and reduced further when compositing over all of the legs. The mesoscale momentum flux is less systematic than the turbulent stress and is more sensitive to the flux averaging scale than the turbulent stress. Sampling and instrumentation problems are briefly discussed, particularly with respect to mesoscale motions.

1. Introduction

Vertical fluxes of heat, moisture, and momentum, and the corresponding exchange coefficients in the bulk aerodynamic formula depend on the choice of the cutoff length scale and flux averaging length scale, either in terms of time or distance, and the method of computing the flux. The ambiguity resulting from the scale dependence of the fluxes can lead to disagreement between observed exchange coefficients, corresponding to uncertainty in the bulk aerodynamic formula.

In numerical models, the so-called subgrid fluxes at each grid point represent transport by all motions having scales less than the grid size, which include not only *turbulent* eddies having scales much smaller than a grid size but also *subgrid mesoscale* motions having scales larger than the size of turbulent eddies but smaller than the grid size. Little is known about fluxes caused or modified by subgrid mesoscale motion. The parameterization of the subgrid mesoscale flux is essentially an unsolved problem. The subgrid flux in numerical models is traditionally assumed to be only turbulent flux parameterized by the bulk aerodynamic formula using similarity theory. The latter is developed from turbulent flux data taken at a point over land under stationary and homogeneous conditions. The relationship between the grid-averaged turbulent flux and the grid-averaged (resolved) mean flow, however, is likely to be different than the relationship between the local turbulent flux and local mean variables. Under homogeneous conditions, the subgrid flux is approximately equal to the area-averaged turbulent flux and subgrid mesoscale fluxes can be neglected. However, subgrid

& NCAR is sponsored by the National Science Foundation.

Corresponding author address: Dr. Jielun Sun, PAOS, University of Colorado, Campus Box 311, Boulder, CO 80309-0311.

TABLE 1. NCAR Electra low-level flight legs.

Leg number	Flight legs	Date (UTC) (mo/d/yr)	Starting time (seconds since 00 UTC)	Ending time (seconds since 00 UTC)	Leg length (s)	Flight height (m)
1	RF01-1	11/15/92	88504	89844	1341	32
2	RF01-2	11/15/92	90770	91673	904	32
3	RF01-3	11/15/92	92186	93157	972	32
4	RF01-4	11/15/92	93952	94677	726	31
5	RF04-1	11/28/92	15142	15869	728	36
6	RF04-2	11/28/92	16094	16878	785	37
7	RF04-3	11/28/92	17104	17840	737	38
8	RF10	12/8/92	69766	70747	982	38
9	RF11-1	12/9/92	74028	75332	1305	38
10	RF11-2	12/9/92	75821	76788	968	36
11	RF11-3	12/9/92	77243	77991	749	38
12	RF11-4	12/9/92	79694	80487	794	36
13	RF12-1	12/10/92	71291	72074	784	37
14	RF12-2	12/10/92	72947	73559	613	39
15	RF14-1	12/14/92	75608	76361	754	39
16	RF14-2	12/14/92	76384	77019	636	39
17	RF16-1	12/16/92	94646	95494	849	39
18	RF16-2	12/16/92	95882	96636	755	36
19	RF16-3	12/16/92	97192	97847	656	39
20	RF16-4	12/16/92	98223	98970	748	36
21	RF16-5	12/16/92	99410	100173	764	38
22	RF16-6	12/16/92	100537	101713	1177	39
23	RF17-1	1/9/93	84961	85934	974	33
24	RF17-2	1/9/93	86548	87686	1139	34
25	RF17-3	1/9/93	88388	89323	936	31
26	RF20	1/14/93	89377	89982	606	34
27	RF22	1/17/93	94506	95154	649	33

mesoscale fluxes and subgrid mesoscale modulation of the turbulent flux can be generated by the surface heterogeneity (Sun and Mahrt 1994), gravity and convection waves (Hauf and Clark 1989), and subgrid mesoscale variations of unknown origins (Geernaert et al. 1987; Mahrt and Gibson 1992). When this subgrid mesoscale flux is systematic and large in magnitude, it must be included in the subgrid flux parameterization.

In this paper, the scale dependence of the vertical flux is examined using observed aircraft data taken over the western equatorial Pacific Ocean. The observations used in this paper are described in section 2. The dependence of fluxes on the cutoff length scale and fluxing averaging length scale is examined and the scale for turbulent eddies is objectively defined in section 3. The validity of the bulk aerodynamic formula is examined as a function of the cutoff and flux averaging length scales in section 4. Based on the characteristics of the scale dependence of fluxes, the subgrid mesoscale flux is further partitioned into large eddy and mesoscale fluxes in section 5, where flight leg lengths are assumed to be grid sizes. Conclusions are given in section 6.

2. Data

The Tropical Ocean Global Atmosphere (TOGA) Coupled Ocean–Atmosphere Response Experiment (COARE) was conducted from 1 November 1992 to 28 February 1993 in the western equatorial Pacific Ocean (TCIPO 1992). During TOGA COARE, the NCAR aircraft Electra flew 32 flight missions to study boundary layer fluxes and convective systems. The data were recorded on board the Electra at two sampling rates: 1 Hz and 20 Hz. The fluxes in this study are calculated using the 20-Hz data. The aircraft speed is about 100 m s^{-1}. Among the 32 missions, all low-level flights that satisfy the following criteria are selected in this study.

1) Elevation of flight legs is between 30 m and 40 m. Choosing low-level flights minimizes errors in the estimate of the surface flux due to vertical divergence of flux between the surface and flight level and due to random flux sampling errors at higher levels. The latter increases with height for a limited flight length due to increasing size of vertical transporting eddies with height. In addition, the turbulent flux may be more strongly modulated by larger-scale motions at higher levels in the boundary layer (LeMone 1976). The difference of flight levels between any adjacent sampling points is required to be less than 5 m, and the difference between the maximum and minimum flight heights for each flight leg is less than 25 m.

2) The roll and pitch angles are restricted to ranges of −4° to 4°, and 0° to 3°, respectively.

3) The minimum flight leg length is 600 s, which is about 60 km.

Table 1 lists the 27 flight legs from 10 Electra flight missions that satisfy the above criteria. Among the selected 27 legs, the leg-averaged wind speeds range from 1.3 to 8 m s^{-1}, and the flight levels range from 31 to 38 m above sea level. In order to compare momentum flux for all the legs, the x axis is rotated into the direction of the mean wind so that the leg-averaged wind component along the y axis is zero. To varying degrees, there are clouds above all 27 legs. Surface radiation temperature (SST) is generally homogeneous and less correlated with air vertical motions except leg 8, where the SST dropped about 1°C coincident with an increase in the aircraft-measured liquid water content to 0.06 g m^{-3}, implying light precipitation. The SST drop may have been caused by a cool fresh water lens from recent rainbands. Precipitation was also observed for flight legs 23 and 24. Due to the possible errors caused by sensor wetting for part of the flight leg, the flight legs 23 and 24 will be eliminated from the statistical analyses of leg-averaged fluxes.

Some "spikes" that appear in the fast response data due to instrument noise are removed using a procedure similar to Højstrup (1993). Here, a spike is defined as a point in the data series that differs from a 1-km mean by more than four standard deviations. Spikes are replaced using linear interpolation between good data values. The flux differences between the despiked and raw data are less than 1%.

The low-frequency horizontal velocity components are corrected for drift using GPS. The vertical velocity component relies on the averaged horizontal pressure within an integration loop of about 60 s. The integration and pressure update is done for every point. Strong horizontal variation of pressure within the integration loop may cause the vertical motion to drift from its true value. However, the patterns of low-frequency vertical velocity in several organized convective systems look physically plausible. Also, for flight legs without obvious mesoscale organization of convection based on radar and satellite images, fluxes based on the mesoscale vertical motion are small. Nonetheless, the accuracy of the mesoscale vertical motions in this study is not known.

3. Scale dependence of fluxes

a. Cutoff length scale and flux averaging length scale

In this study, fluxes are calculated using the eddy-correlation method. Any perturbation, $\phi'(x; L)$, is defined as the deviation at x from the local mean, $\bar{\phi}(L)$, where the overbar refers to a uniformly weighted mean or a box mean with averaging distance L, the *cutoff length scale.* Here x is the distance along a flight track. Mathematically, this high pass filtering operation is written as

$$\phi'(x; L) = \phi(x) - \bar{\phi}(L). \quad (1)$$

Here, $\bar{\phi}(L)$ can be calculated as a *nonoverlapping* mean; that is, the segment of width L for calculation of $\bar{\phi}$ does not overlap with the next segment of width L for calculation of the adjacent $\bar{\phi}$. Therefore, when treated as a nonoverlapping mean, the value of $\bar{\phi}$ within each segment of width L is a constant, while the perturbation value varies with x. Although $\bar{\phi}$ is constant within each nonoverlapping segment, the value of $\bar{\phi}$ may vary in space from segment to segment over the flight leg. Alternatively, $\bar{\phi}(L)$ can be calculated as a *running mean;* that is $\bar{\phi}(L)$ is the mean value of ϕ averaged over the window width L centered at x. The running mean $\bar{\phi}(L)$ varies with x.

The vertical *instantaneous flux,* $w'\phi'$, at any point x, is uniformly averaged over a distance λ, the *flux averaging scale,* to form the flux $[w'\phi']$. The flux averaging is a low pass operation and is indicated by square brackets. To satisfy strict Reynolds averaging criteria, the cutoff length L for perturbations should be equal to the flux averaging length λ for each nonoverlapping segment of the flight leg. In this case, $[w'\phi'] = \overline{w'\phi'}$. However, fluxes are sometimes calculated with $\lambda > L$ in order to obtain large-scale area-averaged fluxes or a larger sample of the flux.

If $\lambda = nL$, where n is an integer and the instantaneous flux within the flux averaging window λ is based on nonoverlapping means, then the Reynolds averaging criteria are satisfied for the fluxes within each nonoverlapping segment. The flux within each segment will be referred to as the local flux. If the instantaneous flux within the flux averaging window λ is based on the running mean, then the Reynolds averaging criteria are not satisfied since the mean value is different for every x. In the running mean case, $\overline{\phi'} \neq 0$; therefore the cross terms, such as $\overline{w'\bar{\phi}}$, are not equal to zero. However, for a time series where $\bar{\phi}(x) \approx$ constant, the sample size of local fluxes based on running means can be dramatically increased compared to those based on nonoverlapping means, although the samples are no longer independent. In addition, the running mean flux can be computed at each point for displaying the spatial variability of the flux. Therefore, some of the analyses in this study are based on the running mean. In this study we examine $[w'\phi']$ as a function of both L and λ.

b. Flight leg-averaged flux as a function of cutoff length scale L

To study fluxes as a function of the cutoff length scale L, the perturbation variable ϕ' is calculated based on the running mean $\bar{\phi}(x, L)$, and the instantaneous vertical flux, $w'\phi'$, is calculated and then averaged over the entire flight leg.

The leg-averaged flux, represented by $[w'\phi']$, is composited over all the legs listed in Table 1 except

legs 23 and 24 (section 2) and plotted in Fig. 1. The composite leg-averaged flux increases rapidly with L for L less than 1 km for heat, moisture, and momentum (Fig. 1). The rate of the flux increases with increasing L, reaches a maximum value at $L \approx 100$ m for heat and moisture fluxes, and at $L \approx 70$–80 m for the momentum flux (thick solid lines in Fig. 1), corresponding to maximum flux contribution from these scales to the composite leg-averaged flux. The rate of increase for momentum vanishes at about 1 km, while significant fluxes of heat, and particularly moisture, occur on scales larger than 1 km. As L increases beyond $L \approx 1$ km, the increase rate oscillates because the flux for L greater than 1 km may be upward or downward and is less systematic than the flux for scales of less than 1 km. For L less than 1 km, the composite of $[w'\phi']$ probably represents mainly turbulent flux averaged over each leg. For larger L, the composite of $[w'\phi']$ includes not only turbulent flux, but also fluxes caused by motions with horizontal scales larger than turbulent scales but smaller than the flight leg length. The composite leg-averaged flux for $L = 1$ km captures 90% of the leg-averaged flux for all the variables and is, therefore, defined as the *turbulent flux*. The thick dotted lines in Fig. 1 represent the accumulated flux due to all scales smaller than L, analogous to the Ogive technique (Friehe et al. 1991) except here L represents the actual spatial scale instead of wavelength in Fourier space. The composite leg-averaged flux based on nonoverlapping means (not shown) results in similar flux variations with L as in Fig. 1.

The standard deviation of the leg-averaged flux for a given cutoff length L in Fig. 1 (thin lines) demonstrates the variation of the leg-averaged flux between flight legs. The number of samples decreases with increasing L for a given flight leg, and as a result, flux sampling problems for an individual leg becomes large. For the flight legs in this study, we anticipate that the leg-averaged flux will suffer random sampling problems for L larger than about 20 km (Sun and Mahrt

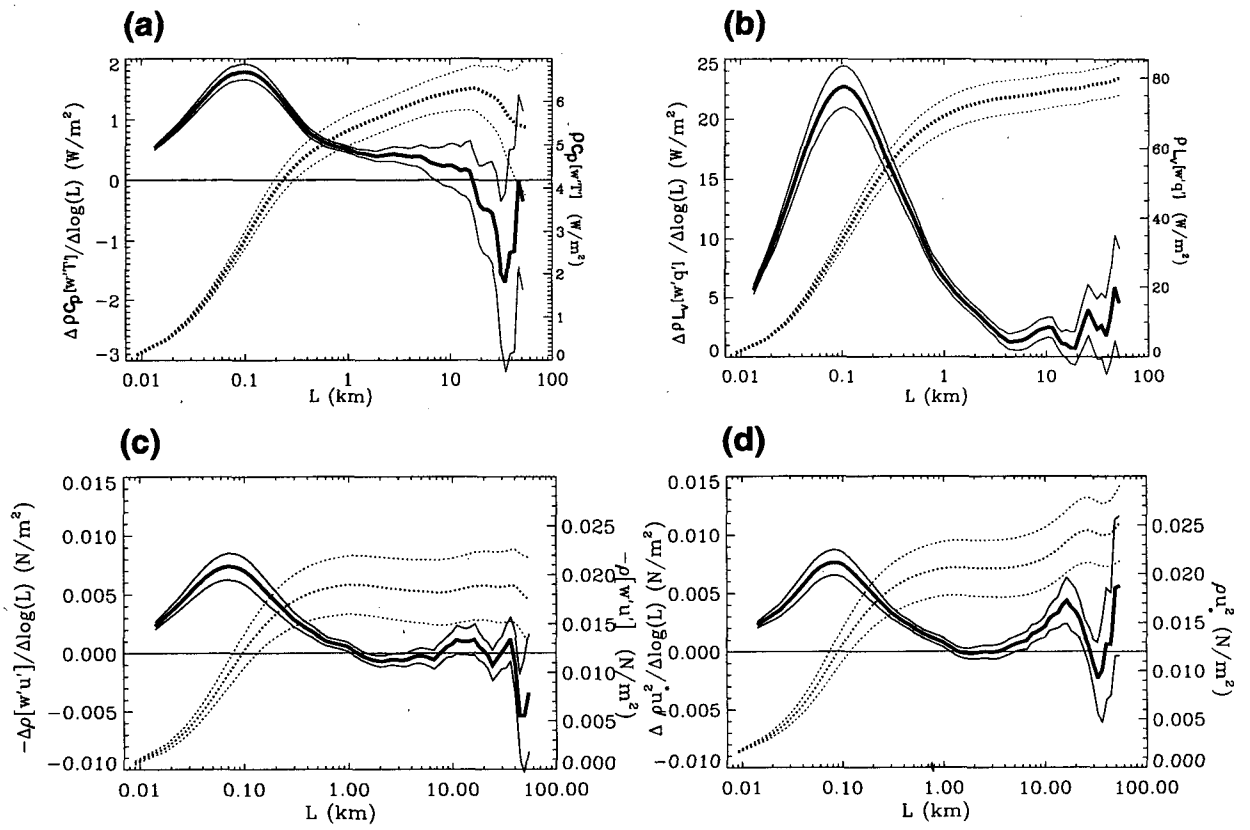

FIG. 1. The composite leg-averaged flux (thick dotted lines, the vertical axes on the right) and the composite change of leg-averaged flux with increasing cutoff scale (thick solid lines, the vertical axes on the left) for (a) sensible heat flux, (b) latent heat flux, (c) momentum flux along the wind direction, and (d) momentum flux. Here ρ, c_p, L_v, T, and q represent air density, the heat capacity of dry air, the latent heat of evaporation, air temperature, and specific humidity, respectively. The flux for a given range between L_1 and L_2 would be equal to the area under the thick solid line between the values of L_1 and L_2. Also shown are plus and minus one standard error for the leg-averaged flux (thin dotted lines) and for the change of the leg-averaged flux with increasing L (thin solid lines). The standard error for the leg-averaged flux is equal to the standard deviation of the leg-averaged fluxes between flight legs divided by the square root of the number of legs. The same definition applies to the standard error of the change of flux with increasing L.

1994). The large variation of the leg-averaged flux between the 25 flight legs for L greater than 5 km (Fig. 1) probably reflects the large sampling error, errors in the measured vertical velocity, and the large variability of mesoscale motions between flight legs. We find that linear detrending does not change the leg-averaged flux for L less than 20 km. In order to avoid distortion of the mesoscale flow, linear detrending is not applied in this study.

For a given flight leg, $[w'\phi'](L)$ is the leg-averaged flux from motions with length scale up to L; therefore the leg-averaged flux due to motions from scale L_1 to L_2 is the difference between $[w'\phi'](L_2)$ and $[w'\phi'](L_1)$. The dependence of the flux on the cutoff scale L for a given flight can be quantified in terms of the standard deviation of $[w'\phi'](L)$ for different values of L, represented as σ. In order to study the flux variation on scales of motions greater than the turbulence, the rapid increase of $[w'\phi'](L)$ for L less than 1 km is excluded in the calculation of the standard deviation of $[w'\phi'](L)$. For a flight leg with little subgrid mesoscale flux, σ will be small. The relative sensitivity of the leg-averaged flux to L for different magnitudes of the flux and for fluxes of different quantities can be measured and compared in terms of σ normalized by $[w'\phi']_{\text{avg}}$, the averaged value of $[w'\phi'](L)$ over a range of L. For each flight leg, the normalized standard deviation is written as

$$S_\phi = \sigma/[w'\phi']_{\text{avg}}, \tag{2}$$

where

$$\sigma = \left(\frac{1}{N}\sum_{L_i}([w'\phi'](L_i) - [w'\phi']_{\text{avg}})^2\right)^{1/2} \tag{3}$$

and

$$[w'\phi']_{\text{avg}} = \frac{1}{N}\sum_{L_i}[w'\phi'](L_i). \tag{4}$$

For simplicity, Eqs. (3) and (4) are evaluated as the leg-averaged fluxes for nonoverlapping windows at discrete values of L,

$$L_i = 2^{i-1}L_{\min}, \quad i = 1, 2, \cdots N. \tag{5}$$

Here, $L_{\min}$ ($\geq$1 km) is the minimum scale for L, determined by the flight leg length L_{leg} and the desired number of segments of width $L_{\min}$ using $L_{\text{leg}}/L_{\min} = 2^{N-1}$ and $L_{\text{leg}} = L_N$.

The quantity S_ϕ indicates the sensitivity of the flux to the cutoff length scale L for a given flight leg for L greater than 1 km. When S_ϕ is small, say $\approx 10^{-1}$ over a given flight leg, there is little difference between the turbulent flux and the leg-averaged flux that includes the flux by all motions up to the scale of the flight leg length (Fig. 2). We may regard the statistics of the fluxes for such flight legs as homogeneous since small mesoscale flux usually corresponds to homogeneous turbulent flux.

The value of S_ϕ exceeds 0.2 (20%) for 7 of the 27 legs for heat, 2 of the legs for moisture, and 6 of the legs for momentum (Fig. 2). Large values of S_ϕ for heat, moisture, and momentum are correlated. For the leg-averaged sensible heat and moisture fluxes where S_ϕ exceeds 0.2 (20%), S_ϕ for heat and moisture fluxes tends to be dominated by the variation of the leg-averaged flux with L between values of 10 km and the flight leg length (Fig. 3). The large variation of $[w'\phi'](L)$ with L in Fig. 3 shows that the leg-averaged subgrid mesoscale flux is sometimes upward so that $[w'\phi'](L)$ increases with L and sometimes downward so that $[w'\phi'](L)$ decreases with L. In general, $[w'\phi'](L)$ does not vary monotonically with L. The variation of $[w'\phi'](L)$ for momentum shows a similar pattern. For almost all the flight legs, the spatial variation of the SST appears to be too small to force atmospheric subgrid mesoscale circulation. We therefore expect that most of the mesoscale flux is due to well-organized mesoscale convective systems (section 3d).

The sensitivity of S_ϕ to the cutoff length scale is greater for the sensible heat flux than for moisture flux in the disturbed cases, where S_ϕ is relatively large (Figs. 2 and 3). Figures 2 and 3 indicate that motions on scales larger than 1 km and smaller than flight leg length have a relatively larger effect on sensible heat flux compared with the moisture flux. Variation of the larger-scale vertical motion is better correlated with variation of the subgrid mesoscale temperature than the subgrid mesoscale specific humidity. Subgrid mesoscale variations of specific humidity are generally small and less systematic. The sensitivity of S_ϕ for momentum is largest for low wind speed, where the turbulent momentum flux is weak (Fig. 4).

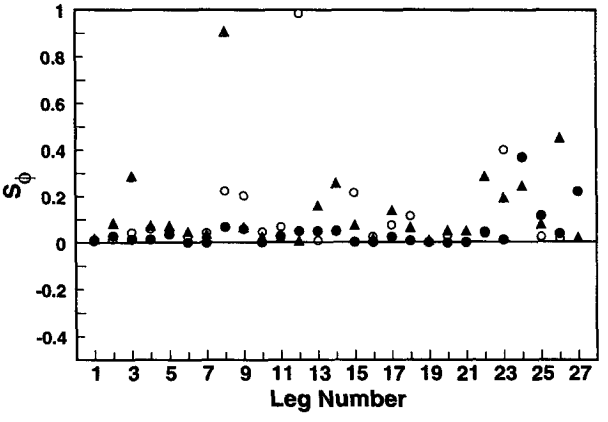

FIG. 2. S_ϕ for heat (open circles), moisture (filled circles), and momentum (triangles) fluxes for all flight legs listed in Table 1. The values of S_ϕ for heat flux are -2.5 and 1.2 for leg 24 and leg 27, respectively, and are off-scale.

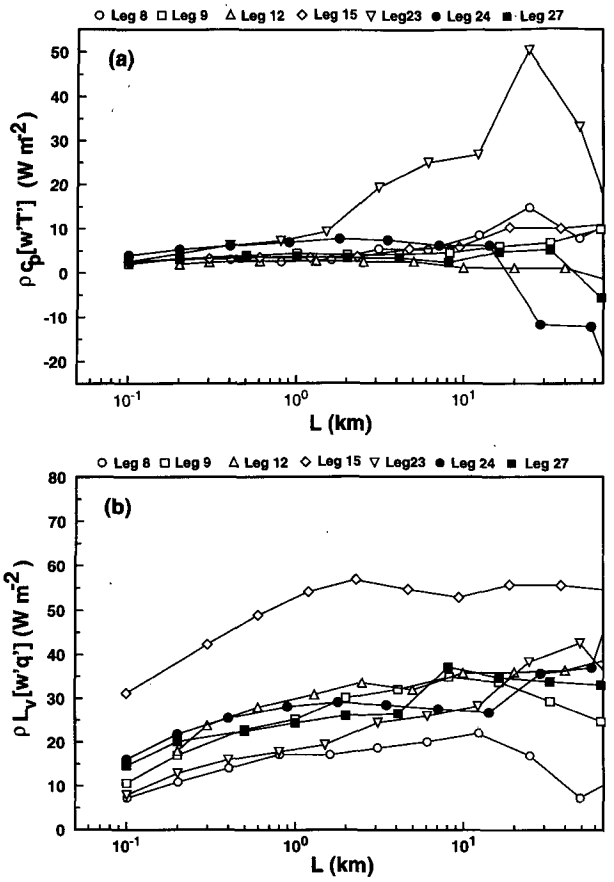

FIG. 3. (a) Leg-averaged sensible and (b) latent heat fluxes as a function of L for the seven flight legs where S_ϕ exceeds 0.2 (20%) for sensible and latent heat fluxes.

The results in Figs. 2–4 also suggest that the flux due to subgrid mesoscale motions is relatively more important when the turbulent flux is weak. The large variation of leg-averaged heat flux for legs 23 and 24 in Fig. 3 is related to a sudden wind shift with precipitation and decrease of air temperature associated with precipitation as mentioned in section 2.

c. *Fluxes as a function of flux averaging length scale* λ

For a given flight leg, the nonoverlapping leg-averaged scalar fluxes, such as heat and moisture fluxes, are independent of the flux-averaging scale λ; that is,

$$([w'\phi'](L, \lambda))_{\text{leg-average}} = [w'\phi'](L, \lambda = L_{\text{leg}}), \quad (6)$$

where λ on the left side is less than the flight leg length L_{leg}. However, for the stress magnitude defined as

$$\tau = \rho u_*^2 = \rho([w'u']^2 + [w'v']^2)^{1/2} \quad (7)$$

both the leg-averaged nonoverlapping momentum flux components, $[w'u']$ and $[w'v']$, are functions of cutoff length scale L and averaging length scale λ. Here, τ is the stress magnitude and ρ is the air density. The direction of the stress is not always opposite to the wind direction. The crosswind momentum flux can be caused by local differences between the wind and wind shear and by lack of equilibrium between the turbulence and mean flow in the surface layer. As the flux averaging scale λ increases, cancellation due to sign reversal of one or both of the momentum flux components reduces the magnitude of the vector averaged stress. As a result,

$$([w'u']^2(L, \lambda) + [w'v']^2(L, \lambda))^{1/2}_{\text{leg-average}} \geqslant ([w'u']^2(L, \lambda = L_{\text{leg}}) + [w'v']^2(L, \lambda = L_{\text{leg}}))^{1/2}. \quad (8)$$

In order to demonstrate the dependence of the momentum flux on both cutoff length scale and flux averaging scale, the nonoverlapping local momentum flux is calculated with variable L and λ, where λ can be smaller than L for the purpose of complete coverage of λ variation, and averaged over the entire flight leg. The dependence of the stress magnitude on the flux averaging length scale λ can be illustrated in terms of the difference of the stress magnitude between two flux averaging length scales, λ = 1 km and λ = 72 km for all flight legs with sufficiently long flight leg lengths (Fig. 5). The stress magnitude at λ = 72 km is less than that at λ = 1 km for all values of L, corresponding to positive values in Fig. 5. As the cutoff scale L increases, the stress difference also increases. This increase indicates that the stress direction associated with larger L is more variable and, therefore, the stress for large L is more vulnerable to cancellation and magnitude reduction with large values of the flux averaging scale λ. In other words, the turbulent stress vector is more systematically directed opposite to the mean wind shear when compared to the more variable subgrid mesoscale stress vectors (more in section 5).

Figure 5 also shows that even for the turbulent stress alone ($L \approx 1$ km), increasing the flux averaging scale from λ = 1 km to λ = 72 km reduces the stress magnitude by 1 or 2 10^{-2} N m^{-2}, which is typically a reduction of 50% or more. This implies that the turbulent stress, based on leg-averaged stress components, is significantly smaller than a leg-averaged local stress [Eq. (8)]. The spatial variability of the stress, as measured by the aircraft, is also partly due to random variations of the turbulent stress associated with random spatial variation of the strength and location of the transporting eddies. Since the aircraft essentially measures the instantaneous spatial distribution of the turbulent stress along the flight track, much of this variation would be eliminated by hypothetical time-averaging at all spatial points along the flight track.

d. *Relationship between mesoscale convective systems and the scale dependence of fluxes*

Strong subgrid mesoscale variations in meteorological variables occur in the low-level flights associated

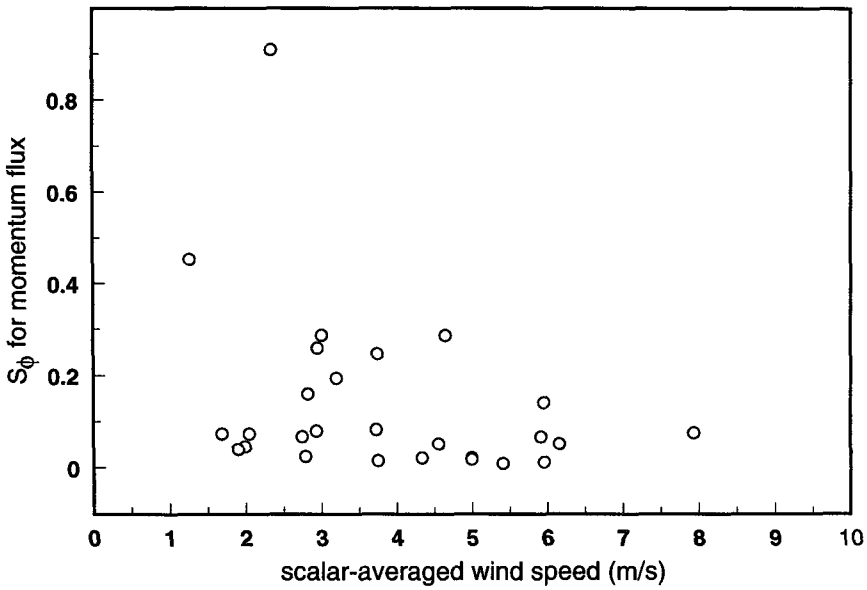

FIG. 4. S_ϕ for momentum flux vs the leg-averaged scalar wind speed for all the low-level flight legs. The leg-averaged scalar wind speed is calculated with the leg-averaged wind speed at each point.

with mesoscale convective cloud bands on the scale of about 30 km, as indicated by radar images in the flight region and large spatial variation of downward solar radiation across the flight leg. The strong scale dependence of fluxes in Fig. 3 is found to be associated with the mesoscale convective systems. One of these examples is flight leg 15 (Fig. 6). For flight leg 15, both air temperature and specific humidity are strongly affected by mesoscale convective systems as indicated by small downward solar radiation (distance between 0 and 30 km in Fig. 6). The air temperature is reduced by roughly 1°–2°C in the region, apparently by evap-

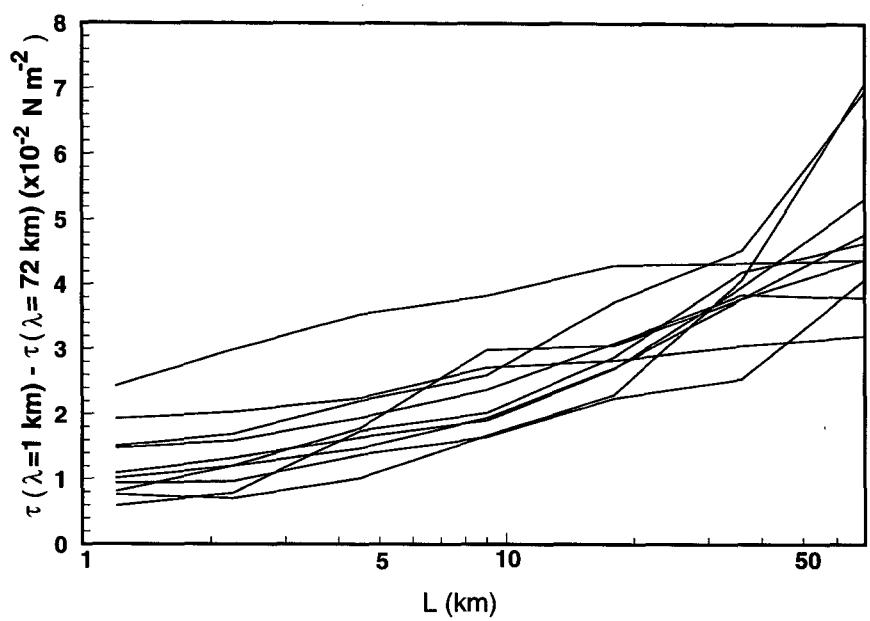

FIG. 5. The difference of stress magnitude τ (10^{-2} N m^{-2}), between two flux averaging lengths λ = 72 km and λ = 1 km as a function of cutoff length scale, L, of the ten flight legs with sufficiently long flight leg length.

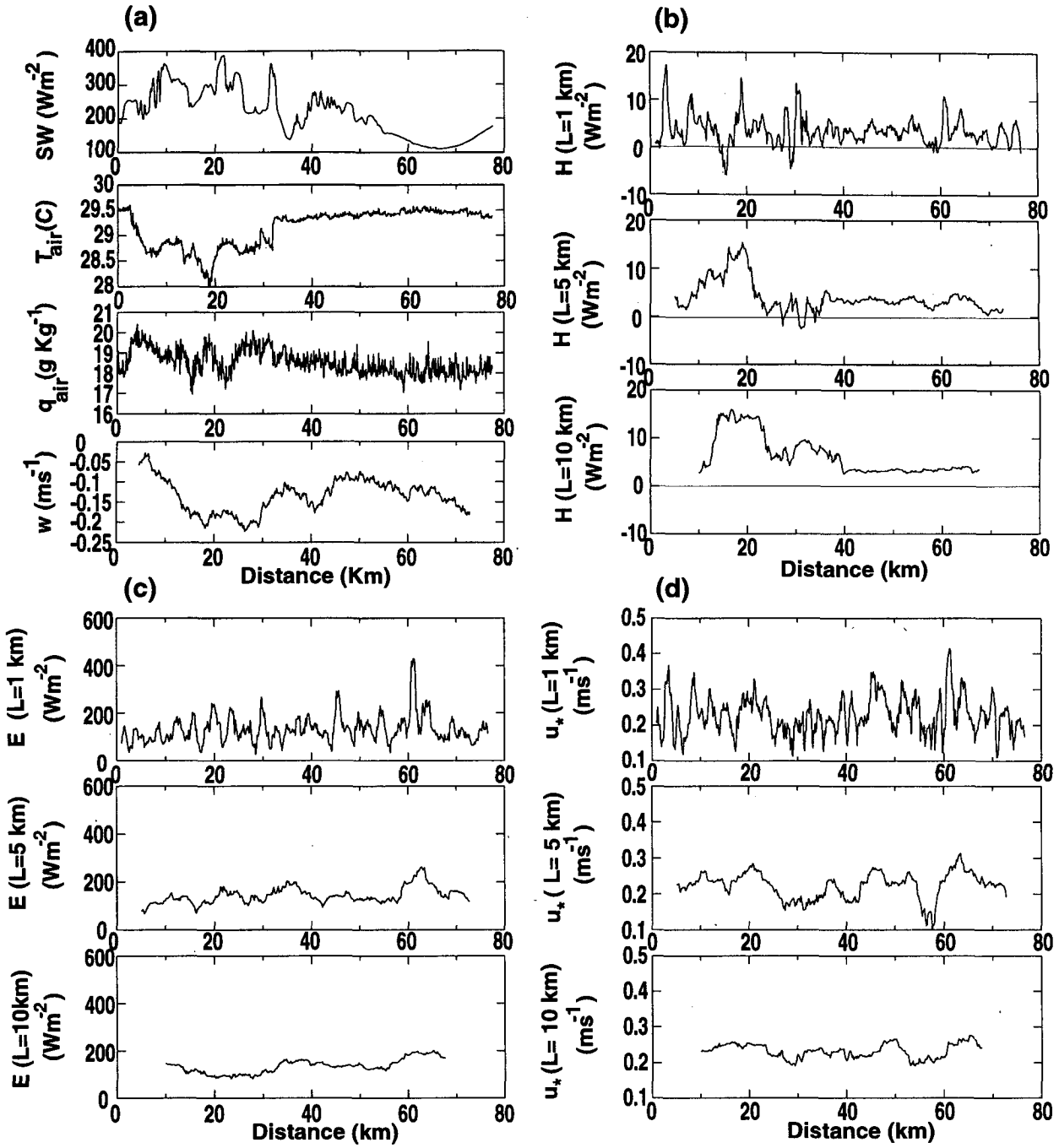

FIG. 6. Flight leg 15. (a) Downward solar radiation SW, air temperature T_{air}, specific humidity q_{air}, and vertical motion w; (b) sensible heat flux (H) for $\lambda = L = 1$, 5, and 10 km as a function of distance along the flight track; (c) latent heat flux (E); and (d) friction velocity (u_*).

oration in the convective downdraft of the mesoscale convective band. The band can be identified on the images from the MIT radar on board the R/V *Vickers*.

The subgrid mesoscale variation of the specific humidity associated with the subgrid mesoscale disturbed conditions is less systematic compared to temperature. The specific humidity in the mesoscale disturbance may be less than or greater than values in the clear air region. For flight leg 15 (Fig. 6), the water vapor content is a little less in the wake of the convective band (from distance of 40 to 80 km in Fig. 6) than in the convective band, which is consistent with convective systems observed by Zipser (1977), Johnson and Nicholls (1983), and Young et al. (1992).

The flux along the flight track for flight leg 15 is calculated using the unweighted running mean with $L = \lambda = 1$, 5, and 10 km (Fig. 6). The change of the sensible heat flux with increasing cutoff length from 1 to 10 km in Fig. 6 indicates that the mesoscale convective bands are associated with large values of the sensible heat flux due to motions between 1 and 10 km. The relationship between the mesoscale convective system and moisture and momentum fluxes at the three values of L is not as clear as that for sensible heat flux in Fig. 6.

In contrast to the mesoscale disturbances associated with cloud bands, the air temperature and specific humidity seem to be less affected by smaller-scale (less than 5 km) scattered clouds for the undisturbed cases. The ocean surface temperature strongly affects the near-surface air temperature and specific humidity due to the large thermal inertia of water and mesoscale motions have less effect on leg-averaged fluxes for undisturbed cases.

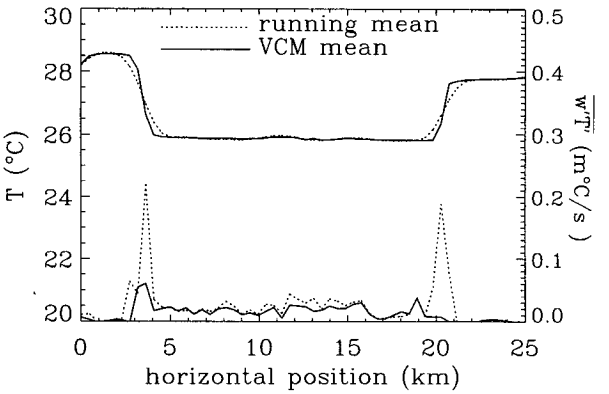

FIG. 7. The comparison between the VCM mean (solid lines) and running mean (dashed lines) for air temperature and sensible heat flux for part of leg 23.

e. *Effects of sharp fronts on calculation of fluxes*

The magnitude of mesoscale flux depends on definition and the method used to calculate the mesoscale flux particularly at the locations with sharp changes of wind and temperature associated with fronts and edges of mesoscale updrafts and downdrafts. With application of a running mean and other conventional filtering techniques, the sharp changes in the mesoscale flow are partly captured as spurious turbulent fluctuations (high-pass part). More specifically, turbulent fluxes computed from deviations from the simple running mean can exhibit large superficial peaks at locations of sudden mesoscale changes. In this subsection, fluxes based on the box mean are examined by using an adaptive filter, the variance conserving multiresolution (VCM) filter, where the effective averaging length shrinks at locations of sharp mesoscale changes. The VCM filter (Howell and Mahrt 1994) can reduce this scale ambiguity by capturing the sharp mesoscale changes as part of the mesoscale (low-pass) flow. The VCM filter is able to capture the sharp changes as mesoscale motion yet retain all of the turbulent flux because its effective window width shrinks in the vicinity of the sharp mesoscale changes.

For example, consider a 25-km segment of leg 23 shown in Fig. 7, which is sufficiently separated from precipitation occurring earlier in the leg to avoid sensor wetting error. This segment contains sharp temperature jumps associated with a mesoscale convective band. Here, the 1-km running mean inadvertently increases the segment-averaged turbulent flux by about 100% due to the artificial peaks of turbulent flux at the edge of the mesoscale downdraft (see Fig. 7). The artificial peaks increase rapidly with increase of the window width of the running mean. Reducing the window width of the running mean to 500 m eliminates these artificial peaks and the flux difference between the VCM filter, and the simple running mean becomes less than 1% for the 25-km segment. However application of this 500-m window width to other records would sometimes omit significant turbulent fluxes that occur on scales between 500 m and 1 km.

Although the VCM adaptive filter is ideal for case studies involving sharp mesoscale changes, this filter is more complex than the simple running mean. Since the VCM filter and the simple running mean with 1-km window width produce similar flux values for most of the legs, we retain the simple box mean for systematic calculations involving all of the legs. The 1-km window width seems to be a reasonable balance between minimizing the artificial flux peaks yet retaining most of the turbulent flux, whereas for subgrid mesoscale flux the magnitude varies according to the method used.

f. *Subgrid mesoscale fluxes*

As mentioned in the introduction, the subgrid flux at each grid point in numerical models should include not only the turbulent flux, but also subgrid mesoscale fluxes as well. As seen in the previous subsections, a large value of the subgrid mesoscale flux is likely associated with mesoscale convective systems. In this section, we investigate characteristics of the subgrid mesoscale flux.

To make an analogy to numerical models, a total flight leg length is considered as a transact across a grid box, and the leg-averaged flux for the cutoff length equal to the total flight leg length is assumed to be an estimate of the subgrid flux. The subgrid flux includes perturbations on all scales smaller than the grid size, here the flight leg length. In order to separate the subgrid turbulent flux from the subgrid mesoscale flux, we express the subgrid flux as

$$[w''\phi''] \equiv [(w - [w])(\phi - [\phi])], \qquad (9)$$

where the square brackets represent the averaging over the grid size L_{leg} and the subgrid perturbation ϕ'' is the deviation of ϕ from the grid average value $[\phi]$. The subgrid perturbation ϕ'' can be further decomposed into the turbulent perturbation ϕ' from the segment mean $\bar{\phi}$ for $L = 1$ km and the subgrid mesoscale deviation of $\bar{\phi}$, ϕ^*, from the grid average value $[\phi]$ (Fig. 8). That is

$$\phi'' = \phi^* + \phi', \tag{10}$$

where

$$\phi^* \equiv \bar{\phi} - [\phi]. \tag{11}$$

Notice here that ϕ' represents the turbulent perturbation for $L = 1$ km, whereas ϕ' in the previous subsections represents deviations from an arbitrary value of L. For nonoverlapping segments, $\bar{\phi}$ is constant within each segment. Therefore, ϕ^* only varies between segments.

Substituting Eq. (10) into Eq. (9), the subgrid flux $[w''\phi'']$ becomes

$$[w''\phi''] = [(w' + w^*)(\phi' + \phi^*)] = [w'\phi'] + [w^*\phi^*] + [w'\phi^*] + [w^*\phi']. \tag{12}$$

If the decomposition satisfies Reynolds averaging, that is, $\bar{\phi}$ is nonoverlapping, the last two terms on the right-hand side are zero since Eq. (12) can be written as

$$[w''\phi''] = \Big(\sum_i^N \overline{w'\phi'} + \sum_i^N w_i^*\phi_i^* + \sum_i^N \phi_i^*\overline{w'} + \sum_i^N w_i^*\overline{\phi'}\Big)/N. \tag{13}$$

Because $\overline{\phi'} = 0$ and ϕ^* is constant within each segment, the last two terms are zero. Therefore, Eq. (12) becomes

$$[w''\phi''] = [w'\phi'] + [w^*\phi^*]. \tag{14}$$

The first and second terms on the right-hand side of Eq. (14) represent the turbulent and subgrid mesoscale fluxes averaged over the grid scale, respectively.

The magnitude of the local subgrid mesoscale moisture flux (w^*q^*) for each segment can be larger than the instantaneous turbulent flux ($w'q'$) at any point, even when there are no obvious mesoscale variations of downward solar radiation, such as occurs with flight leg 22 (Fig. 9). For most of the low-level flight legs, however, the leg-averaged subgrid mesoscale moisture flux ($[w^*q^*]$) is smaller than the leg-averaged turbulent flux ($[w'q']$) due to the cancellation of upward and downward local subgrid mesoscale fluxes. In contrast the turbulent moisture flux is consistently upward. Similar cancellation of local subgrid mesoscale fluxes is found for sensible heat and momentum fluxes.

For some individual flight legs with organized mesoscale convective systems, the magnitudes of the subgrid mesoscale heat, moisture, and momentum fluxes can be more than 50%, 20%, or 20% of the subgrid heat, moisture, or momentum fluxes, respectively. However, for homogeneous flights, the subgrid fluxes are dominated by grid-averaged turbulent fluxes. This is consistent with the findings of Esbensen and McPhaden (1995) that there is little difference between the flux calculated with daily averaged mean variables and the daily average of the flux calculated from hourly TAO buoy data in the absence of precipitating mesoscale convective systems. Both our results and the study by Esbensen and McPhaden (1995) indicate that the subgrid flux is dominated by grid-averaged turbulent flux under homogeneous conditions over oceans.

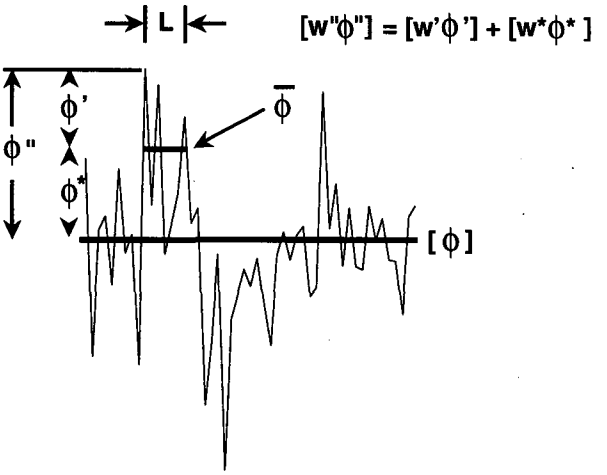

FIG. 8. The relationship between the turbulence ϕ', mesoscale ϕ^*, and subgrid perturbations ϕ''.

4. Relationship between fluxes and local mean variables as a function of cutoff length scale L and flux averaging length scale λ

Surface fluxes are commonly estimated using bulk aerodynamic formulas. The bulk aerodynamic formula is based on similarity theories for turbulent fluxes in the surface boundary layer under stationary and homogeneous conditions. Due to the scale dependence of the flux, the correlation between fluxes and local mean variables in the bulk relationship may be a function of cutoff length scale L and flux averaging scale λ. The scale dependence of the bulk aerodynamic formula is studied in this section.

To summarize the behavior of the bulk formula as a function of the cutoff length scale, $L = 1$, 5, and 10 km are selected. Each flight leg is divided into 1-, 5-, or 10-km segments. The fluxes and the mean variables in the bulk aerodynamic formula, such as the wind speed, air–sea temperature difference, and the difference between the saturated specific humidity using SST and the specific humidity observed from the aircraft, are calculated for each segment and for all flight legs ex-

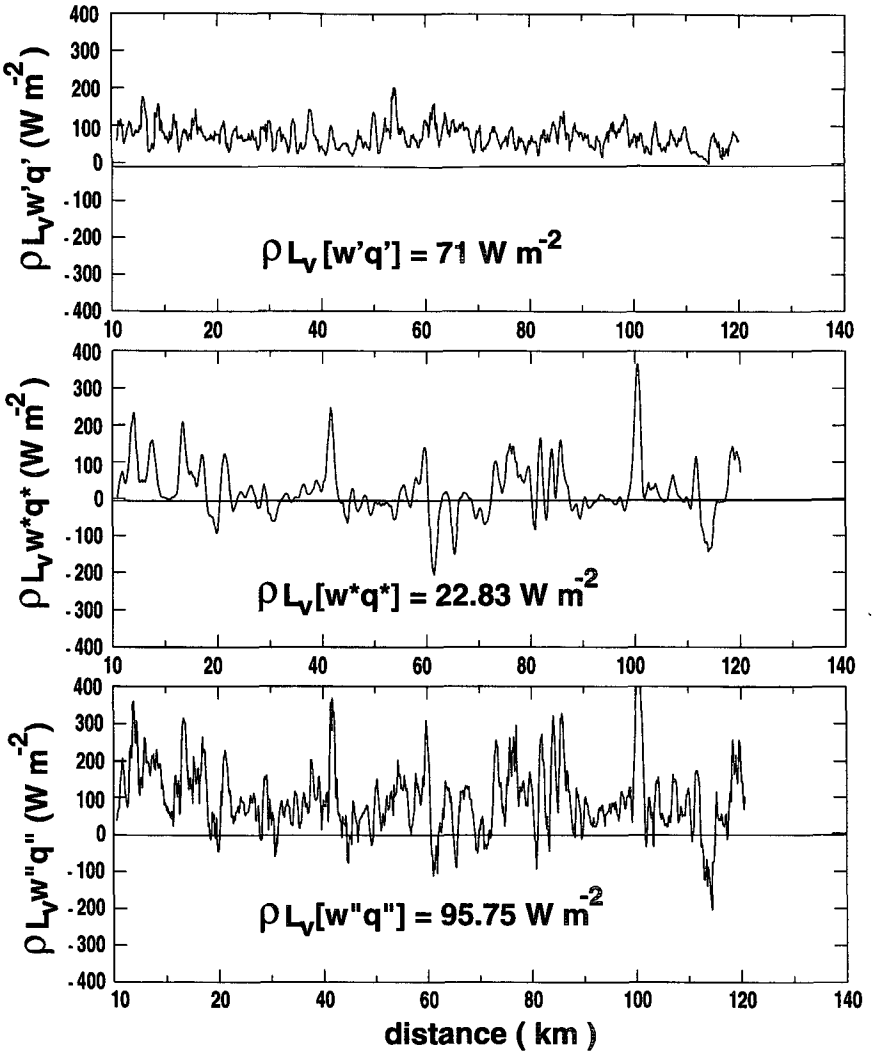

FIG. 9. Variations of smoothed instantaneous turbulence ($w'q'$ for L = 1 km), subgrid mesoscale ($w^*q^* = w''q'' - w'q'$, for 1 km < scale of motions < L_{leg}), and subgrid ($w''q''$ for $L = L_{leg}$) latent heat fluxes along flight leg 22. The values of leg-averaged fluxes are also shown.

cept legs 23 and 24. Figure 10 shows the linear correlation coefficients between the fluxes and the segment-mean variables in the bulk aerodynamic formula. For the cutoff length equal to the flux averaging length (the dark dashed lines in Fig. 10), the highest correlation coefficients between fluxes and the products of the mean variables in the bulk formula do not appear to have an obvious preferred cutoff length scale among L = 1, 5, and 10 km. Note here, the flux at L represents all motions with scales up to L. As L increases, the random sampling error for turbulent fluxes for each segment of width L decreases. Therefore, the correlation between fluxes and mean variables could increase. However, increasing L also includes more nonturbulent motions that are not described by the bulk aerodynamic method and acts to decrease the correlation.

As the averaging length λ for the fluxes and the mean variables increases, the random flux error, due to limited data sample in each segment, is reduced (Khalsa and Businger 1977). Thus the correlation between the fluxes and the product of the mean variables in the bulk formula increases with λ for all L. The highest correlation occurs for L = 1 km. Assuming the stability-caused variation of the exchange coefficient is small due to small difference of air–sea temperature, Fig. 10 shows that the flux based on L = 1 km best represents the turbulent flux and that the bulk aerodynamic relationship deteriorates when the cutoff scales become greater than 1 km.

As the flux averaging length continues to increase beyond values used here, the modulation of mesoscale motions on the turbulent flux may start to reduce the

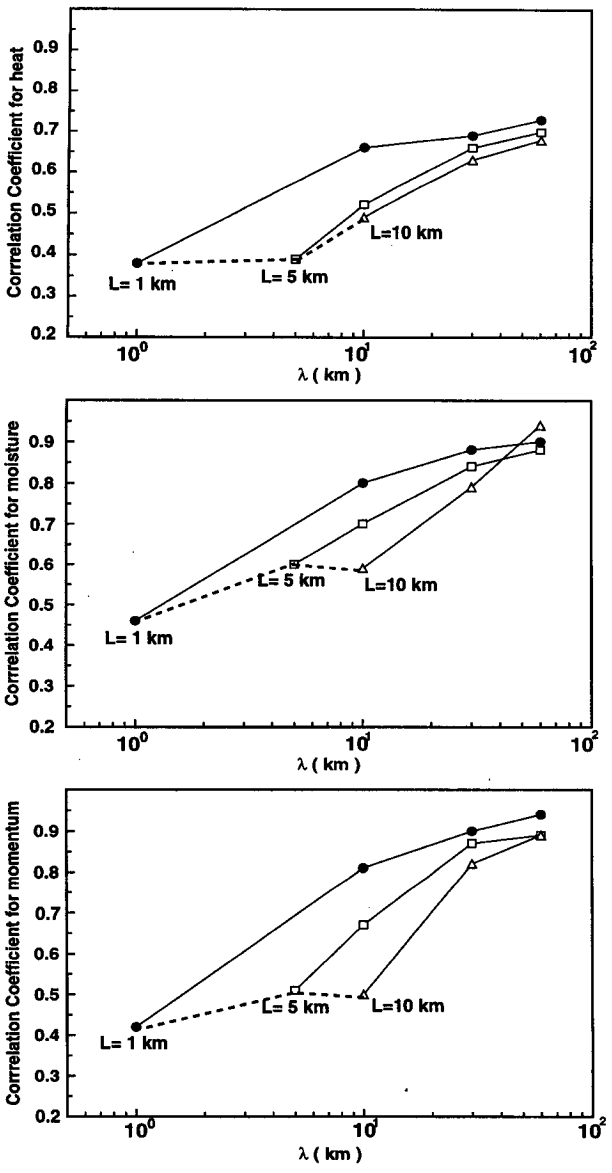

FIG. 10. The correlation coefficients as a function of averaging length λ for L = 1 (filled circles), 5 (squares), and 10 km (triangles) segments from all flight legs in Table 1. Top: the correlation coefficients between the sensible heat flux and the product of the mean wind and the air–sea temperature difference. Middle: the correlation coefficients between the moisture flux and the product of the mean wind and the difference between saturated specific humidity using SST and the specific humidity from aircraft observations. Bottom: the correlation coefficients between the square of the friction velocity and the square of the mean wind. The thick dashed lines represent L = λ.

correlation between the turbulent flux and the mean variables in the bulk formula. The mean variables and turbulent flux may vary from place to place corresponding to the modulation by mesoscale motions. Therefore, the correlation between the space-averaged mean variables and the space-averaged turbulent flux may be smaller than the correlation between local mean variables and local turbulent flux.

5. Leg-averaged fluxes from three classes

a. Classification

Figure 1 has shown that the leg-averaged flux increases dramatically and systematically with increasing cutoff length scale L up to about 1 km. Furthermore, the bulk aerodynamic relationship is better behaved for fluxes from scales $\leq$ 1 km in that the flux is better correlated with the mean flow (section 4). The leg-averaged momentum flux is nearly independent of averaging scale as L increases from 1 to 5 km. The contribution of the flux due to motions on scales between 5 km and flight leg length may become quite large but not in a systematic way and may reverse sign between different legs (section 3). In order to further study the variation of fluxes with L from 1 km to the flight leg length, the leg-averaged subgrid flux can be divided into three classes based on the general characteristics of the flux variation as a function of L in Fig. 1:

1) turbulence, due to motions with scales less than 1 km;
2) large eddies, due to motions with scales less than 5 km and greater than 1 km;
3) mesoscale, due to motions with scales greater than 5 km and less than the flight leg length.

The flux for the large eddies is $[w'\phi']$ (L = 5 km) minus $[w'\phi']$ (L = 1 km). The mesoscale flux, as defined above, is estimated as $[w'\phi']$ ($L = L_{\text{leg}}$) minus $[w'\phi']$ (L = 5 km). Here, the large eddies include motions with a horizontal scale larger than the boundary layer depth but smaller than traditional mesoscale motions. These large eddies are characterized by little vertical motion and usually contribute less than the surface turbulent flux but are quite coherent. The large eddies and mesoscale eddies may include "inactive eddies" (Townsend 1976; Högström 1990), roll vortices (LeMone 1976; Mourad and Brown 1990), the organizing effect of larger convective circulation above the surface layer (Williams and Hacker 1993), cumulus-induced boundary layer motions, small mesoscale instabilities (Emanuel 1983), gravity waves and convection waves coupled to boundary layer motions (Hauf and Clark 1989; Balaji et al. 1993), and entrainment by large eddies at the top of the boundary layer (Barnes et al. 1980; Mahrt 1991).

With the above classification, the leg-averaged turbulent fluxes of heat, moisture, and momentum are much larger than both the leg-averaged large eddy and mesoscale fluxes for the 25 flight legs (Fig. 11). The leg-averaged turbulent flux is always downgradient (from large mean values to small mean values), the leg-averaged large eddy flux is mostly downgradient, and the mesoscale flux can be in either direction. The

mesoscale flux is caused by transient features and is less systematic than the large eddy flux, which in turn is less systematic than the turbulent flux.

The turbulent stress in Fig. 11 is generally directed opposite to the direction of the wind vector. The momentum flux due to mesoscale motions in Fig. 11 is random in direction. On average, both large eddy and mesoscale stresses tend to be perpendicular to the wind direction and the turbulent stress. The updrafts and downdrafts associated with mesoscale motions may be significantly deeper than the boundary layer. Therefore, the mesoscale stress that acts upon vertical wind shear over a deeper layer can be quite different from that near the surface. However, based on limited aircraft soundings close to the location of the selected low-level flights, a well-defined relationship between the mesoscale stress at the flight level and vertical wind shear over a deeper layer is not obvious. The direction difference between the turbulent, large eddy, and mesoscale stresses may reflect different vertical "mixing" mechanisms for different scales of motion.

b. Compositing fluxes

This subsection examines composite fluxes for the three categories in section 5a obtained by averaging over the 25 Electra flight legs (legs 23 and 24 have been omitted due to possible instrument wetting). This calculation does not provide a true climatology of TOGA COARE fluxes, which would require averaging over a much larger dataset including a wider range of conditions. Our purpose in this subsection is to provide a simple summary of the scale dependence of fluxes and to identify systematic relationships among the 25 flight legs. In addition to summarizing the scale dependence of fluxes, averaging over all of the legs reduces the influence of random flux sampling errors assuming the environmental conditions at the TOGA COARE region are similar from day to day. Averaging all the low-level flights provides a measure of the importance of fluxes in the three categories in the statistical sense for applications to numerical models.

Spatial variation of the flux along a flight leg can be caused by random flux errors because of undersampling within flux averaging windows. Under homogeneous conditions, increasing the flux averaging length λ increases the sample size of turbulent eddies and improves the relationship between the flux and mean flow variables as shown in section 4. Under the influence of mesoscale convective systems, turbulent eddies can be modified by mesoscale motions. Then, increasing the averaging length scale includes turbulent eddies under different environmental conditions, thus complicating the relationship between the flux and mean flow. Increasing the cutoff scale L increases the range of eddy sizes contributing to the flux, which increases the flux sampling error for large L for a given flight leg.

The magnitude of the fluxes averaged over all of the 25 flight legs are shown in Table 2 for the three flux categories (section 5a). Also shown in Table 2 is the estimated relative random flux error between legs. The relative random flux error is calculated as the standard deviation of the leg-averaged flux, $[w'\phi']$, from different legs, normalized by $[w'\phi']_{avg}$ and the square root of the total number of flight legs. Table 2 shows that the random sampling error increases with the scale of the motion and is smallest for moisture fluxes and largest for momentum fluxes, particularly the crosswind momentum flux.

The turbulent momentum flux along the leg-averaged wind direction is much larger in magnitude than the crosswind turbulent momentum flux, and the latter varies much more than the former. Therefore, the composite turbulent stress is approximately opposite to the wind direction (Fig. 12). In contrast, the stress due to large eddy and mesoscale motions is not opposite to the wind direction. These stresses tend to be small and the relative flux errors for both large eddy and mesoscale stress are large. The composite mesoscale stress is dominated by large mesoscale stress from several flight legs (Fig. 11) associated with well-organized convective cloud bands.

The fact that the relative errors for the large eddy momentum flux components are larger than for the large eddy sensible heat and moisture fluxes suggests that the large eddy sensible heat and moisture fluxes are more systematic and vary less between different events than the large eddy momentum flux. Furthermore, a longer sampling period may be required to measure momentum fluxes compared to heat and moisture fluxes (Lenschow and Stankov 1986; Mahrt and Gibson 1992) due to greater spatial variability of momentum fluxes (Baljaars and Holtslag 1991). The large relative error for all mesoscale fluxes indicate even larger flux sampling problems and substantial variation of mesoscale situations between different flight legs. Additionally, the mesoscale vertical velocity may be contaminated by instrument drift due to horizontal pressure variations, as discussed in section 2. However, the negative mesoscale sensible heat flux and positive mesoscale moisture flux in Table 2 agree with results from the southern extremity of the Atlantic trade winds (BOMEX 1969) reported by Donelan and Miyake (1973) and Grossman (1973).

The large eddy latent heat flux is much smaller than the turbulent latent heat flux but is larger than the turbulent sensible heat flux. The relative random flux error for the large eddy heat and moisture fluxes are larger than those of the turbulent fluxes, but they still remain less than 20%. Therefore, the composite large eddy heat and moisture fluxes are significant, albeit small. Since the size of the vertical transporting eddies increases with height, the relative importance of the large eddy and mesoscale fluxes also increase with height (Williams et al. 1996). The large eddy fluxes from even low-level flights must be included in estimates of the surface flux, although this inclusion increases the

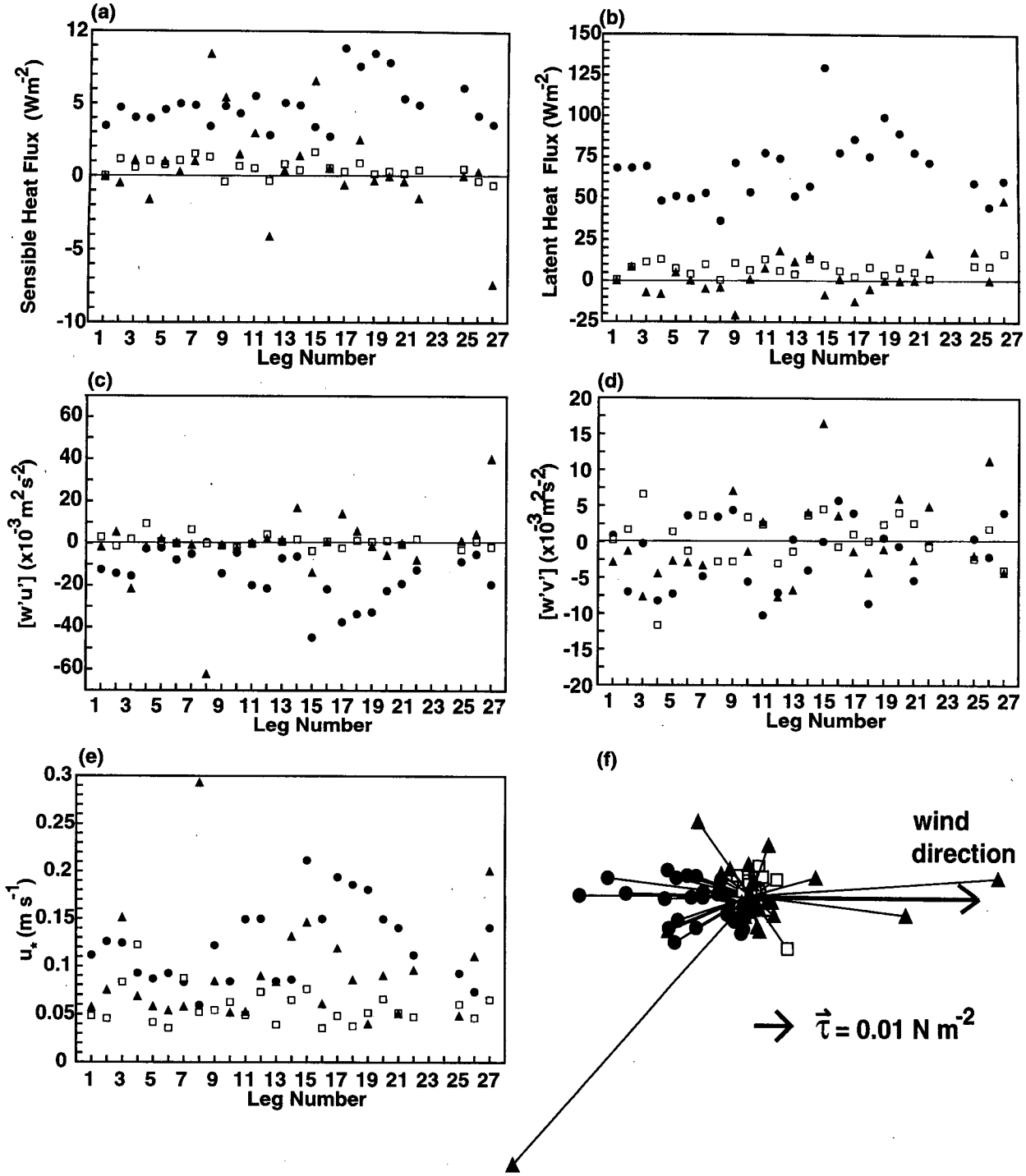

FIG. 11. (a) Sensible heat, (b) latent heat, (c) momentum fluxes in the along- and (d) crosswind directions, (e) frictional velocity, and (f) stress vectors due to turbulence (filled circles), large eddies (squares), and mesoscale motions (triangles) for the 26 low-level flight legs listed in Table 1. The mesoscale heat flux (-55 W m^{-2}) for leg 24 is off-scale. Leg 23 is eliminated due to possible errors caused by instrument wetting.

TABLE 2. Statistics of fluxes for the three classes.

Flux type	Class	$[w'\phi']$ averaged over the 25 flight legs	Relative random error
Sensible heat	turbulence	5.06 (W m^{-2})	0.06
Sensible heat	large eddies	0.85 (W m^{-2})	0.17
Sensible heat	mesoscale	−1.45 (W m^{-2})	1.48
Latent heat	turbulence	68.38 (W m^{-2})	0.05
Latent heat	large eddies	9.73 (W m^{-2})	0.09
Latent heat	mesoscale	7.56 (W m^{-2})	0.65
$[w'u']$ (in-wind direction)	turbulence	−18.71 ($\times 10^{-3}$ N m^{-2})	0.14
$[w'u']$ (in-wind direction)	large eddies	0.72 ($\times 10^{-3}$ N m^{-2})	0.97
$[w'u']$ (in-wind direction)	mesoscale	2.04 ($\times 10^{-3}$ N m^{-2})	2.35
$[w'v']$ (in-wind direction)	turbulence	−1.8 ($\times 10^{-3}$ N m^{-2})	0.61
$[w'v']$ (in-wind direction)	large eddies	0.72 ($\times 10^{-3}$ N m^{-2})	1.20
$[w'v']$ (in-wind direction)	mesoscale	−2.52 ($\times 10^{-3}$ N m^{-2})	1.18

scatter of the computed fluxes based on aircraft data. Betts et al. (1990) and Sun and Mahrt (1994) also found that failure to include scales larger than 5 km leads to underestimation of the surface flux over land in unstable conditions. Of course over land, the daytime boundary layer is deeper, the surface is more heterogeneous, and motions on scales larger than a few kilometers are expected to be stronger. Nevertheless, the inclusion of larger-scale transport will be important in comparisons between shipboard and aircraft measurements.

6. Conclusions

Heat, moisture, and momentum fluxes are computed from low-level Electra aircraft data collected during TOGA COARE over the western tropical Pacific Ocean. In the absence of organized mesoscale convective systems, the fluxes of heat, moisture, and momentum are approximately independent of the cutoff length scale used to compute the perturbations. For undisturbed conditions, the mesoscale flux is relatively important only for cases of weak turbulent fluxes, as occurs with weak wind conditions. Well-organized mesoscale convective systems lead to large horizontal variations of air temperature, specific humidity, and wind. The mesoscale flux is significant in such mesoscale convective systems, and the flux estimates are sensitive to the choice of flux averaging length for momentum and sensitive to the cutoff length for all fluxes. A number of independent considerations all suggest choosing L to be about 1 km in order to isolate turbulent fluctuations from larger-scale variations.

A mesoscale convective system can significantly modulate surface turbulent flux and meteorological variables underneath the convective system, as occurred in the Cessna aircraft observations in TOGA COARE reported by Williams et al. (1996). The mesoscale flux transported directly by the mesoscale circulation associated with the convective system can transport heat in the opposite direction of turbulent flux and, therefore, complicates the estimate of the subgrid flux.

The mesoscale flux is large only in mesoscale convective systems, and the local values of the mesoscale flux in space can be positive or negative and upgradient or downgradient. The large eddy fluxes, and particularly the mesoscale fluxes, are not well correlated to the wind speed and bulk air–sea differences. Therefore, these fluxes cannot be well represented by the conventional bulk aerodynamic formulas. As expected, averaging the mesoscale flux over entire flight legs or multiple flight legs reduces its relative importance. In contrast, the sign of the turbulent flux does not usually change between flight legs. Nonetheless, even after averaging over all 25 flight legs, the large eddy latent heat flux is larger than the turbulent sensible heat flux and, therefore, cannot be ignored in constructing a surface energy balance over the ocean even at 35 m above the sea. The composite large eddy sensible heat and moisture fluxes are statistically significant. Consequently, aircraft data can underestimate the surface flux if the large eddy contributions are not included. The importance of mesoscale fluxes normally increases with height in the boundary layer. The larger-scale fluxes are expected to become more important higher in the boundary layer (Chou and Furguson 1991; Williams et al. 1996).

For the TOGA COARE flight legs investigated here, the mesoscale stress tends to be more random than the

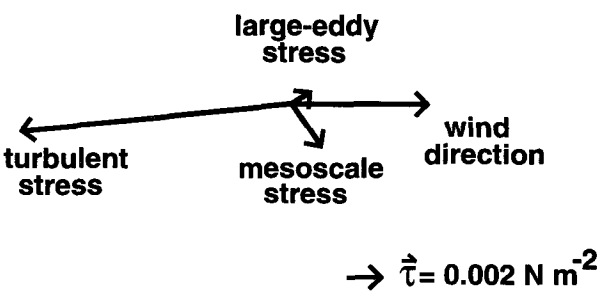

FIG. 12. Vector-averaged stress for turbulent, large eddy, and mesoscale motions for the 25 flight legs.

turbulent stress in both magnitude and direction. With weak winds or well-organized mesoscale convective activity, the momentum flux is particularly sensitive to the averaging scales. This is partly because the direction of the large eddy and mesoscale stress are quite variable so that these stress values are reduced by vector averaging and the amount of reduction increases with averaging scale. Although there is uncertainty on the absolute value of mesoscale vertical motion from aircraft measurements, the results presented in this paper qualitatively agree with the conclusions based on tower measurements by Mahrt et al. (1996). Nonetheless, more work is required on the reliability of aircraft measured vertical motions on the mesoscale.

Acknowledgments. Jielun Sun carried out part of this work while at Oregon State University and Saint Louis University. The discussions with Alastair Williams, Jorg Hacker, Tim Crawford, and David Rogers are greatly appreciated. The authors gratefully acknowledge helpful comments from the reviewers. This material is based upon work supported by the National Science Foundation's Climate Dynamics Program under Grant ATM-9313588 and by the Air Force Office of Scientific Research under Grant F49620-93-1-0497.

REFERENCES

Balaji, V., J.-L. Redelsperger, and G. P. Klaasen, 1993: Mechanisms for the mesoscale organization of tropical cloud clusters in GATE Phase III. Part I: Shallow cloud bands. *J. Atmos. Sci.*, **50,** 3571–3589.

Baljaars, A. C., and A. A. M. Holtslag, 1991: Flux parameterization over land surfaces for atmospheric models. *J. Appl. Meteor.*, **30,** 327–341.

Barnes, G., G. Emmitt, M. LeMone, and S. Nicholls, 1980: The structure of a fair weather boundary layer based on the results of several measurement strategies. *Mon. Wea. Rev.*, **108,** 349–364.

Betts, A. K., R. L. Desjardins, J. I. Macpherson, and R. D. Kelly, 1990: Boundary-layer heat and moisture budgets from FIFE. *Bound.-Layer Meteor.*, **50,** 109–138.

Chou, S.-H., and M. P. Ferguson, 1991: Heat fluxes and roll circulations over the western gulf stream during an intense cold-air outbreak. *Bound.-Layer Meteor.*, **55,** 255–281.

Donelan, M., and M. Miyake, 1973: Spectra and fluxes in the boundary layer of the trade-wind zone. *J. Atmos. Sci.*, **30,** 444–464.

Emanuel, K. A., 1983: On the dynamical definition(s) of 'mesoscale.' *Mesoscale Meteorology—Theories, Observations and Models,* D. K. Lilly and T. Gal-Chen, Eds., Reidel, 1–12.

Esbensen, S. K., and M. J. McPhaden, 1996: Enhancement of tropical ocean evaporation and sensible heat flux by atmospheric mesoscale systems. *J. Climate,* **9**(11), 2307–2325.

Friehe, C. A., and Coauthors, 1991: Air–sea fluxes and surface-layer turbulence around a sea-surface front. *J. Geophys. Res.*, **96,** 8593–8609.

Geernaert, G. L., S. E. Larsen, and F. Hansen, 1987: Measurements of the wind stress, heat flux and turbulence intensity during storm conditions over the North Sea. *J. Geophys. Res.*, **92,** 13 127–13 139.

Grossman, R. L., 1973: An aircraft investigation of turbulence in the lower layers of a marine boundary layer. Ph.D. dissertation, Colorado State University, 69 pp. [University Microfilms No. 74-5422. Ann Arbor, MI.]

Hauf, T., and T. L. Clark, 1989: Three-dimensional numerical experiments on convectively forced internal waves. *Quart. J. Roy. Meteor. Soc.*, **115,** 309–333.

Högström, U., 1990: Analysis of turbulence structure in the surface layer with a modified similarity formulation for near neutral conditions. *J. Atmos. Sci.*, **47,** 1949–1972.

Højstrup, J., 1993: A statistical data screening procedure. *Meas. Sci. Technol.*, **4,** 153–157.

Howell, J. F., and L. Mahrt, 1994: An adaptive multiresolution data filter: Applications to turbulence and climate time series. *J. Atmos. Sci.*, **51,** 2165–2178.

Johnson, H. J., and M. E. Nicholls, 1983: A composite analysis of the boundary layer accompanying a tropical squall line. *Mon. Wea. Rev.*, **111,** 308–319.

Khalsa, S. J. S., and J. A. Businger, 1977: The drag coefficient as determined by the dissipation method and its relation to intermittent convection in the surface layer. *Bound.-Layer Meteor.*, **12,** 273–297.

LeMone, M. A., 1976: Modulation of turbulent energy by longitudinal rolls in an unstable planetary boundary layer. *J. Atmos. Sci.*, **33,** 1308–1320.

Lenschow, D. H., and B. B. Stankov, 1986: Length scales in the convective boundary layer. *J. Atmos. Sci.*, **43,** 1198–1209.

Mahrt, L., 1991: Boundary-layer moisture regimes. *Quart. J. Roy. Meteor. Soc.*, **117,** 151–176.

——, and W. Gibson, 1992: Flux decomposition into coherent structures. *Bound.-Layer Meteor.*, **60,** 143–168.

——, D. Vickers, J. Howell, J. Edson, J. Hare, J. Højstrup, and J. Wilczak, 1996: Sea surface drag coefficients in RASEX. *J. Geophys. Res.*, **101,** 14 327–14 335.

Mourad, P. D., and R. A. Brown, 1990: Multiscale large eddy states in weakly stratified planetary boundary layers. *J. Atmos. Sci.*, **47,** 414–438.

Sun, J., and L. Mahrt, 1994: Spatial distribution of surface fluxes estimated from remotely sensed variables. *J. Appl. Meteor.*, **33,** 1341–1353.

TCIPO, 1992: TOGA COARE Operations Plan, TOGA COARE International Project Office. [Available from TCIPO UCAR, P.O. Box 3000, Boulder, CO 80307.]

Townsend, A. A., 1976: *The Structure of Turbulent Shear Flow.* Cambridge University Press, 429 pp.

Williams, A. G., and J. M. Hacker, 1993: Interactions between coherent eddies in the lower convective boundary layer. *Bound.-Layer Meteor.*, **64,** 55–74.

——, H. Kraus, and J. M. Hacker, 1996: Transport processes in the tropical warm pool boundary layer. Part I: Spectral composition of fluxes. *J. Atmos. Sci.*, **53,** 1187–1202.

Young, G. S., D. V. Ledvina, and C. W. Fairall, 1992: Influence of precipitating convection on the surface energy budget observed during a Tropical Ocean Global Atmosphere pilot cruise in the tropical western Pacific Ocean. *J. Geophys. Res.*, **97,** 9595–9603.

Zipser, E. J., 1977: Mesoscale and convective-scale downdrafts as distinct components of squall-line structure. *Mon. Wea. Rev.*, **105,** 1568–1589.